CONDENSED MATTER PHYSICS

# Optical generation of high carrier densities in 2D semiconductor heterobilayers

Jue Wang[1]*, Jenny Ardelean[2]*, Yusong Bai[1]*, Alexander Steinhoff[3], Matthias Florian[3], Frank Jahnke[3], Xiaodong Xu[4], Mackillo Kira[5†], James Hone[2†], X.-Y. Zhu[1†]



**Controlling charge density in two-dimensional (2D) materials is a powerful approach for engineering new electronic phases and properties. This control is traditionally realized by electrostatic gating. Here, we report an optical approach for generation of high carrier densities using transition metal dichalcogenide heterobilayers, $WSe_2/MoSe_2$, with type II band alignment. By tuning the optical excitation density above the Mott threshold, we realize the phase transition from interlayer excitons to charge-separated electron/hole plasmas, where photoexcited electrons and holes are localized to individual layers. High carrier densities up to $4 \times 10^{14}$ $cm^{-2}$ can be sustained under both pulsed and continuous wave excitation conditions. These findings open the door to optical control of electronic phases in 2D heterobilayers.**

## INTRODUCTION

Two-dimensional (2D) transition metal dichalcogenides (TMDCs) are emerging platforms for exploring a broad range of electronic, optoelectronic, and quantum phenomena. These materials feature strong Coulombic interactions, making them ideal for studying highly correlated quantum phenomena as a function of charge carrier density. Seminal demonstrations include, among others, charge density waves and superconductivity in $TiSe_2$ and $MoS_2$ by electrostatic gating (*1*–*4*). These exciting demonstrations have been possible due to the high charge carrier densities (~$10^{14}$ $cm^{-2}$) achievable with ionic liquid gating. Under bias, a capacitive electrical bilayer is formed between the charge carriers in the 2D material and counter ions in the liquid. Among the limitations of using a liquid as dielectric is that controlling charge carrier density requires gate switching near room temperature, but the appearance of interesting electronic phases occurs mostly upon cooling on hour time scales under the gate bias. Alternatively, in TMDC type II heterobilayers, photoexcited electrons and holes separate on femtosecond time scales (*5*, *6*) to form oppositely charged monolayers. While these spatially separated electrons and holes form Coulomb-bound interlayer excitons (*7*–*10*), the insulating exciton gas can be transformed to conducting charge-separated electron/hole (e/h) plasmas if excitation density is increased to above the Mott threshold ($n_{Mott}$) (*11*, *12*), as illustrated schematically at the top of Fig. 1 for the $WSe_2/MoSe_2$ heterobilayer studied here. The Mott transition has been observed in optically excited monolayer and bilayer $WS_2$ (*13*), but the electron and hole plasmas exist in the same material, which remains charge neutral. In contrast, TMDC heterobilayers host spatially separated electrons and holes with long lifetimes (*7*–*10*, *14*). Therefore, these systems offer a unique opportunity to control high carrier densities in individual 2D monolayers. In this case, the resulting e/h bilayer across the heterointerface in the presence of photoexcitation, particularly under continuous wave (CW) conditions, resembles the capacitive electric bilayer in an ionic-gated 2D material. Here, we use photoluminescence (PL) spectroscopy and time-resolved (TR) reflectance spectroscopy to demonstrate optically driven Mott transition from interlayer exciton to charge-separated e/h plasmas in the $WSe_2/MoSe_2$ heterobilayer. The experimental findings are supported by calculations from quantum theory. The achieved carrier density is as high as $4 \times 10^{14}$ $cm^{-2}$, more than two orders of magnitude above the Mott density.

## RESULTS

### Experiments: Mott transition from interlayer exciton to charge-separated plasmas

We use transfer stacking to form $WSe_2/MoSe_2$ heterobilayers encapsulated by hexagonal boron nitride (h-BN), with the two TMDC monolayers aligned within the light cone (*15*) for radiative interlayer exciton emission (twist angle $\theta = 4° \pm 2°$ from *K*/*K* or *K*/*K*′ stacking), with a dark heterobilayer sample with $\theta = 13° \pm 2°$ (from *K*/*K* or *K*/*K*′ stacking) as control (see fig. S1 for optical images and figs. S2 and S3 for monolayer alignment). The $WSe_2$ and $MoSe_2$ monolayers are exfoliated from flux-grown single crystals, each with defect density <$10^{11}$ $cm^{-2}$, two orders of magnitude lower than in commonly used commercial crystals (*16*). This is critical for suppressing defect-mediated nonradiative recombination previously seen to dominate TMDC heterobilayers (*6*) and for sustaining high excitation density in the charge-separated e/h plasmas. All measurements are carried out with the samples at 4 K in a liquid helium cryostat. The spectroscopic measurements include steady-state PL with CW excitation ($h\nu$ = 2.33 eV), TRPL with pulsed excitation ($h\nu$ = 2.33 eV; pulse width, 150 fs), and transient reflectance spectroscopies with pulsed excitation (hν = 1.82 eV; pulse duration, 150 fs) (see fig. S4 for the experimental setup). At both excitation photon energies, we calculate the absorptance (percentage of incident light absorbed; see fig. S6) to be 8% at the low excitation density limit based on the reported dielectric functions of $WSe_2$ and $MoSe_2$ monolayers (*17*). We carefully calibrate experimental electron/hole density, $n_{eh}$, by including the saturation of absorptance from self-consistent Maxwell semiconductor Bloch equation calculations (see figs. S8 and S9 and table S1). Under the experimental conditions used here, we find the measurements completely reproducible, i.e., there is no sample damage due to laser excitation.

[1]Department of Chemistry, Columbia University, New York, NY 10027, USA. [2]Department of Mechanical Engineering, Columbia University, New York, NY 10027, USA. [3]Institute for Theoretical Physics, University of Bremen, 28334 Bremen, Germany. [4]Department of Physics and Department of Materials Science and Engineering, University of Washington, Seattle, WA 98195, USA. [5]Department of Electrical Engineering and Computer Science and Department of Physics, University of Michigan, Ann Arbor, MI 48109, USA.
*These authors contributed equally to this work.
†Corresponding author. Email: xyzhu@columbia.edu (X.-Y.Z.); jh2228@columbia.edu (J.H.); mackkira@umich.edu (M.K.)

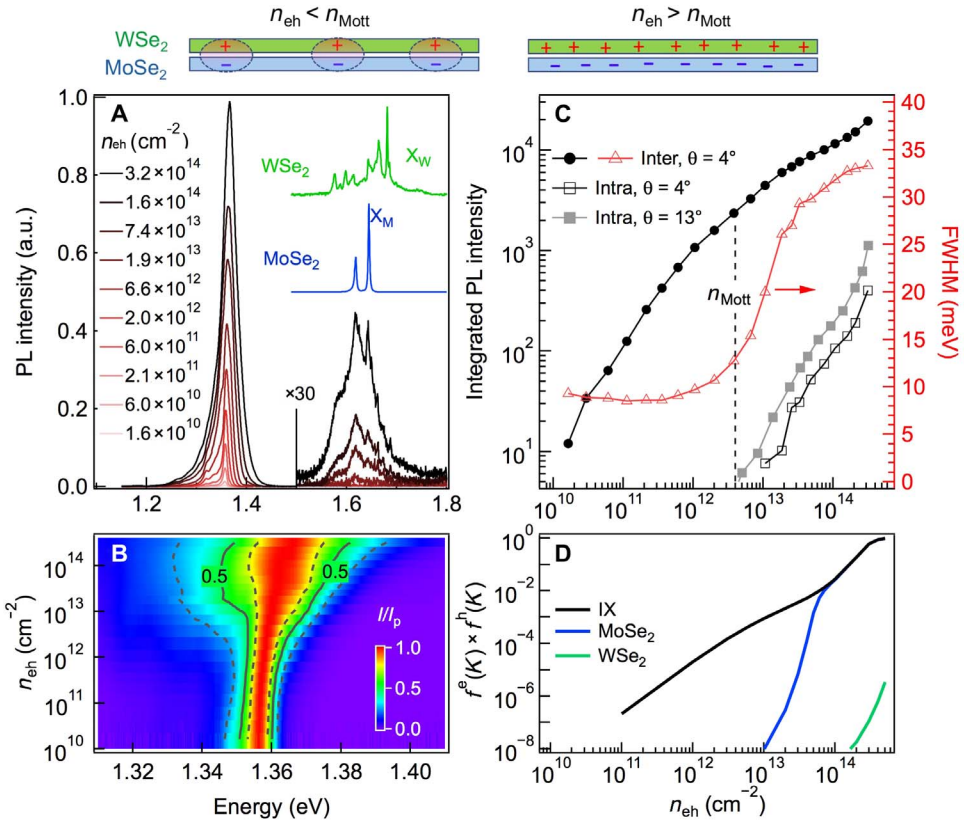


**Fig. 1. Excitation density–dependent PL and Mott transition in the $WSe_2/MoSe_2$ heterobilayer.** PL spectra (**A**) and intensity-normalized PL spectra (**B**) from a BN-encapsulated $WSe_2/MoSe_2$ heterobilayer with θ = 4° ± 2° angular alignment between the two monolayers. a.u., arbitrary units. The spectra were obtained with CW excitation at hν = 2.33 eV and calibrated excitation densities ($n_{eh}$) between $1.6 \times 10^{10}$ and $3.2 \times 10^{14}$ $cm^{-2}$ at 4 K. The spectral region (hν ≥ 1.51 eV) corresponding to PL emission from monolayers $WSe_2$ and $MoSe_2$ is multiplied by a factor of 30. Also in (A) is PL from monolayer $WSe_2$ (green) and monolayer $MoSe_2$ (blue). Shown on the 2D pseudocolor (normalized intensity, $I/I_P$, where $I_P$ is peak intensity) plot in (B) are contours of 50% (solid curve) and 25 and 75% (dashed curves) of $I_P$. (**C**) Integrated intensities (left axis) of interlayer (1.2 to 1.5 eV, solid black circles) and intralayer (1.51 to 1.80 eV, open black squares) PL emission, full width at half maximum (FWHM) of the interlayer exciton peak (open red triangles, right axis) as a function of $n_{eh}$, and integrated intralayer PL intensities (solid gray squares) from a BN-encapsulated $WSe_2/MoSe_2$ heterobilayer with θ = 13° ± 2° angular alignment. (**D**) Computed joint electron/hole populations in the *K* valleys for interlayer exciton (black) and intralayer excitons in $MoSe_2$ (blue) and $WSe_2$ (green). The top of the figure is a cartoon illustrating the Mott transition in the $WSe_2/MoSe_2$ heterobilayer.

However, damage to other heterobilayer samples has been observed for laser excitation exceeding the upper limit shown here.

Figure 1A shows the CW PL spectra from the $WSe_2/MoSe_2$ heterobilayer with $n_{eh}$ spanning over four orders of magnitude ($1.6 \times 10^{10}$ to $3.2 \times 10^{14}$ $cm^{-2}$), achieved by varying excitation power density from ρ = 0.5 $W/cm^2$ to $1.5 \times 10^5$ $W/cm^2$. We quantitatively calibrate the equilibrium excitation density based on $n_{eh} = F \cdot \sigma \cdot \tau_0$, where $F$ is the incident photon flux, σ is the absorptance, and $\tau_0$ is the population decay time constant determined in TRPL; both σ and $\tau_0$ are numerical functions of $n_{eh}$ (see below) determined systematically through our computations and measurements, respectively. A complete set of spectra with normalized peak intensities is shown for the 1.31 to 1.41 eV region in Fig. 1B. Also shown in Fig. 1A are PL spectra of $MoSe_2$ (blue) and $WSe_2$ (green) monolayers. The former is characterized by the neutral exciton ($X_M$) and the trion, while the latter consists of a series of peaks assigned to exciton ($X_W$), trion, biexciton, etc., in agreement with previous reports (*18*–*21*). At $n_{eh} \leq 1 \times 10^{13}$ $cm^{-2}$ in the heterobilayer, PL from intralayer excitons is completely quenched, while interlayer exciton (IX) emission with $E_{IX} = 1.3566 \pm 0.0005$ eV (at $n_{eh} = 1.6 \times 10^{10}$ $cm^{-2}$) dominates (*7*, *22*). The IX peak grows with $n_{eh}$ and blue shifts only by ~8 meV in the entire excitation density range, as is known for coupled (*23*) and uncoupled (*24*) III–V quantum wells.

To experimentally detect the Mott transition, we plot in Fig. 1C the $n_{eh}$ dependences of the integrated intensities from interlayer PL (solid black circles) and its spectral full width at half maximum (FWHM; open red triangles), along with the intralayer PL (open black squares) integrated over the 1.50 to 1.75 eV energy rage. The interlayer emission peak broadens substantially when the theory-assigned $n_{Mott} = 3 \times 10^{12}$ $cm^{-2}$ (vertical dashed line; see below) is crossed. The corresponding FWHM increases by as much as a factor of four, verifying that excitons (and the narrow linewidth they sustain) are absent above $n_{Mott}$. We also observe that intralayer PL, corresponding to broad emission from $MoSe_2$ and/or $WSe_2$ monolayer(s), reappears and grows for $n_{eh} > 1 \times 10^{13}$ $cm^{-2}$. As the charge-separated e/h plasmas form at $n_{eh} > n_{Mott}$, the band offsets between the two TMDC monolayers are reduced due to both band renormalization and charge separation. The latter can be understood from a simple capacitive model (see "The capacitor model for charge separation across the $WSe_2/MoSe_2$ heterobilayer" section in the Supplementary Materials), which predicts from the e/h charge separation a voltage buildup, $\Delta V_C$. This $\Delta V_C$ can cancel

out the initial ~300 meV band offset (*14*), leading to the repopulation of the conduction (valence) band of $WSe_2$ ($MoSe_2$) and to intralayer radiative recombination. This interpretation is supported theoretically (Fig. 1D), which shows the computed source for PL emission, i.e., the probability of simultaneously finding electrons and holes in the *K* valleys of $WSe_2$ (green), $MoSe_2$ (blue), and between the two monolayers (black). The experimental onset of intralayer PL matches perfectly with the rise in the computed spontaneous emission source for $MoSe_2$, while PL from $WSe_2$ remains suppressed. Further support for this interpretation comes from PL measurement on the control sample of a $WSe_2/MoSe_2$ heterobilayer with $\theta = 13° \pm 2°$ alignment. The large momentum mismatch between the *K* (or *K′*) valleys across the interface means that the interlayer excitons are nonradiative (*10*). We observe no measurable IX emission, but only intralayer PL at $n_{eh} >> n_{Mott}$ (solid gray squares in Fig. 1C; see fig. S10 for the PL spectra).

We determine the lifetimes of interlayer exciton emission using TRPL under pulsed excitation ($h\nu = 2.33$ eV; see fig. S5 for the instrument response function, which gives a time resolution of ~40 ps). Figure 2A shows TRPL data in the broad initial excitation density range of $n_0 = 1.1 \times 10^{10}$ to $6.0 \times 10^{13}$ $cm^{-2}$. The corresponding time-integrated PL spectra (Fig. 2B) are similar to the CW PL spectra in Fig. 1A (see fig. S11 for direct comparisons). The PL decays at low excitation densities ($10^{10-11}$ $cm^{-2}$) are close to single exponentials, with a decay time constant of $\tau_0 = 200 \pm 40$ ns. As $n_0$ increases, particularly above $n_{Mott}$, the PL decay becomes faster and exhibits a major deviation from single exponential. This behavior is expected for plasma luminescence, as demonstrated in various III–V quantum well systems (*25*). Above the Mott transition, luminescence from the e/h plasmas scales approximately with $n_{eh}^2$. In addition, carrier density may decay nonradiatively, e.g., via Auger recombination that scales approximately with $n_{eh}^3$. As a result, PL decays faster at higher carrier densities, but this is difficult to analyze quantitatively due to the varying Auger scattering cross sections resulting from the expected density-dependent Coulomb screening. Figure 2C plots the initial PL decay time constant as a function of $n_0$. Our PL lifetimes are one to two orders of magnitude longer than those of previous reports on $WSe_2/MoSe_2$ heterobilayers (*7*, *22*, *26*), suggesting the suppression of nonradiative recombination in the less defective TMDC samples used here. These long PL lifetimes are essential to reaching excitation density well above the Mott threshold and to obtaining high steady-state $n_{eh}$ under CW excitation, as $n_{eh}$ is proportional to $\tau_0$.

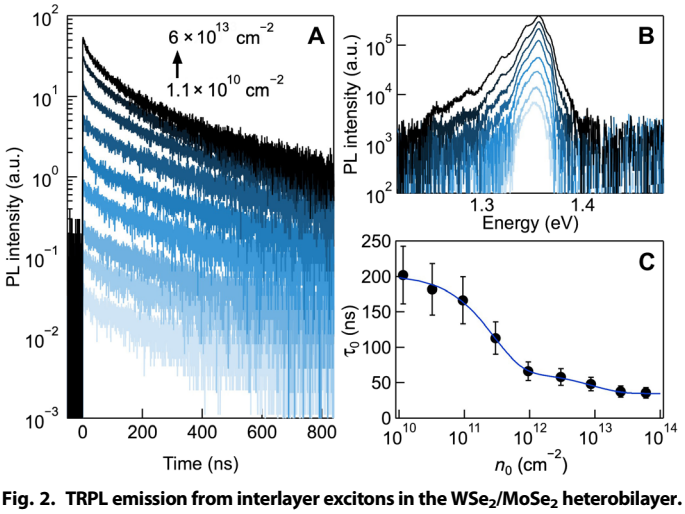


**Fig. 2. TRPL emission from interlayer excitons in the $WSe_2/MoSe_2$ heterobilayer.** The sample at 4 K is excited by pulsed laser ($h\nu = 2.33$ eV; pulse duration, 150 fs). The energy-integrated emission from the interlayer exciton [see spectra in (**B**)] is detected as a function of time (**A**) for initial excitation densities of (from bottom to top) $n_0 = 1.1 \times 10^{10}$, $3.0 \times 10^{10}$, $9.4 \times 10^{10}$, $3.0 \times 10^{11}$, $9.4 \times 10^{11}$, $3.0 \times 10^{12}$, $8.7 \times 10^{12}$, $2.5 \times 10^{13}$, and $6.0 \times 10^{13}$ $cm^{-2}$. (**C**) Initial decay time constants (solid circles) as a function of $n_0$. The solid line is the biexponential fit to the data.

To further explore the properties of charge-separated e/h plasmas in the $WSe_2/MoSe_2$ heterobilayer, we apply transient reflectance spectroscopy (time resolution ~40 fs; see fig. S5), which has been used before to probe excitons and electron-hole (e-h) plasma in TMDC monolayers (*13*) and charge separation in heterobilayers (*5*, *6*). We excite the samples with a 150-fs pulse at 1.82 eV and probe the change in reflectance using broadband white light (1.2 to 1.8 eV). We present transient reflectance, $\Delta R/R_0$, as a function of pump-probe delay ($\Delta t$), where $\Delta R = R - R_0$; $R$ is the reflectance at $\Delta t$, and $R_0$ is the reflectance without the pump. At the 2D limit and low excitation densities, $\Delta R/R_0$ is proportional to transient absorption (*27*). Figure 3 (A to D) shows pseudocolor plots of transient reflectance spectra in a broad range of excitation densities. At $n_0 \leq n_{Mott}$ (Figure 3, A or B), each spectrum is dominated by two prominent photobleaching peaks at ~1.62 and ~1.70 eV, attributed to the reduction in oscillator strength (*6*) of transitions in monolayers $WSe_2$ and $MoSe_2$, respectively. The induced absorption signal (red) on the sides of the main bleaching peaks can be attributed to shifts in intralayer transition energies resulting from competing effects of screening/Pauli blocking of the Coulomb interaction and band renormalization. Note that, at $n_0 < n_{Mott}$, $\Delta R/R_0$ is negligible below 1.5 eV, including the IX region. This is expected as the oscillator strength of the interlayer exciton is two orders of magnitude lower than those of the intralayer excitons in each monolayer (*28*). The absence of $\Delta R/R_0$ signal below 1.5 eV is evident in horizontal cuts at selected $\Delta t$ values, shown for $n_0 = 1.0 \times 10^{11}$ $cm^{-2}$ in (Fig. 3E).

In agreement with the CW results in Fig. 1A, transient reflectance spectra under pulsed excitation reveal plasma formation above the Mott density. At $n_0 = 5.6 \times 10^{12}$ or $3.4 \times 10^{13}$ $cm^{-2}$ (Fig. 3, C and D), the spectra show, in addition to bleaching of intralayer exciton transitions, broad induced absorption extending to the low energy end (~1.3 eV) of the probe window. These broad features are evident in horizontal cuts (spectra) at short pump-probe delays, as shown for $n_0 = 3.4 \times 10^{13}$ $cm^{-2}$ in Fig. 3F. This broad absorption feature is the optical signature of a 2D plasma, which consists of broad induced absorption (positive) extending to the renormalized bandgap and gain (negative) just above the bandgap (*13*, *29*).

While the spectroscopic measurements presented here were obtained at 4 K, we have also carried out PL measurements as functions of both excitation density and temperature up to 48 K (fig. S12). The broadening of PL emission peak across the Mott density is similarly observed at temperatures >4 K. However, the decrease in the excitonic emission intensity with temperature and the broadening due likely to exciton-phonon scattering make the quantitative analysis of the Mott transition less reliable at higher temperatures. Note also that the current manuscript focuses on the transition from interlayer excitons to charge-separated e/h plasmas in the $WSe_2/MoSe_2$ heterobilayer; the Mott transitions from intralayer exciton to e-h plasma have also been observed in transient reflectance spectra for individual $WSe_2$ or $MoSe_2$ monolayer (figs. S13 and S14). In the latter case, the e-h plasma is not charge separated and is overall charge neutral, similar to the observation of Chernikov *et al.* (*13*) on $WS_2$ monolayer and bilayers.

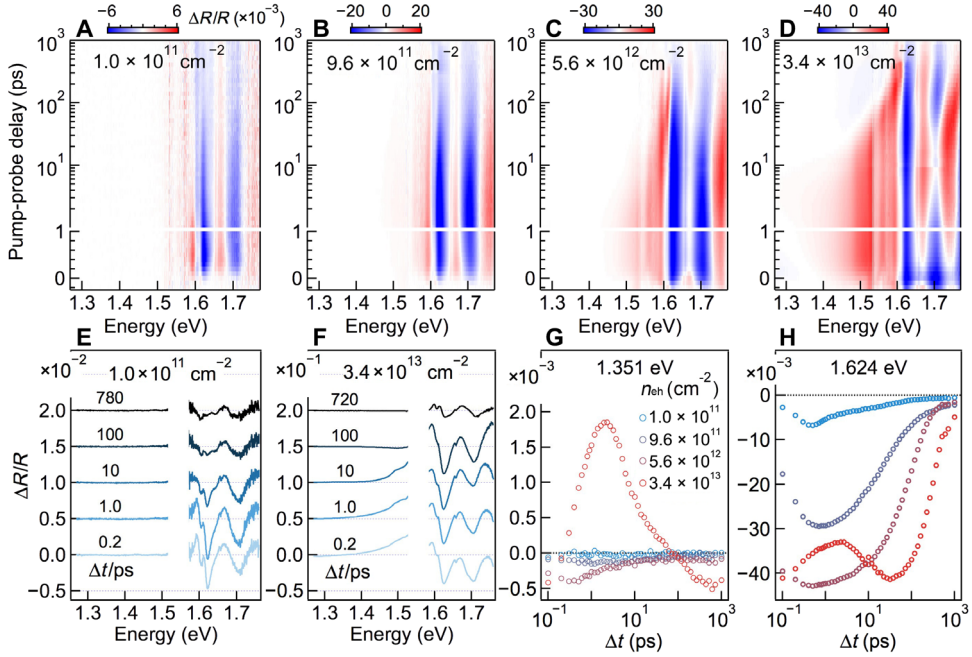


**Fig. 3. Density-dependent transient reflectance spectra from the $WSe_2/MoSe_2$ heterobilayer.** The $WSe_2/MoSe_2$ heterobilayer was excited at hν = 1.82 eV with initial excitation densities of $n_0$ = (**A**) $1.0 \times 10^{11}$, (**B**) $9.6 \times 10^{11}$, (**C**) $5.6 \times 10^{12}$, and (**D**) $3.4 \times 10^{13}$ cm$^{-2}$ at a sample temperature of 4 K. The excited sample is probed with a white light, and the pseudocolor scale is $\Delta R/R_0$ (blue , bleaching; red, induced absorption). Transient reflectance spectra at selected pump-probe delays ($\Delta t$) at $n_0$ = (**E**) $1.0 \times 10^{11}$ and (**F**) $3.4 \times 10^{13}$ cm$^{-2}$ are also shown. The probe regions around 1.55 eV are blocked out due to low intensity and noise from white light which was generated by 1.55-eV laser light. Kinetic profiles obtained from vertical cuts at (**G**) 1.351 and (**H**) 1.624 eV in the 2D pseudocolor plots at the four $n_0$ values.

## Theory: Optical responses of interlayer exciton and e/h plasmas

To calculate the optical properties of photoexcited TMDC heterobilayers, we solve the semiconductor Bloch equations (SBE) (*30*, *31*) for the microscopic interband polarizations $\psi_k^{\mathrm{he}}(t)$

$$i\hbar\frac{d}{dt}\psi_k^{\mathrm{he}}(t) = (\varepsilon_{k,0}^{\mathrm{e}} + \varepsilon_{k,0}^{\mathrm{h}} + \Sigma_{k,\mathrm{SXCH}}^{\mathrm{e}} + \Sigma_{k,\mathrm{SXCH}}^{\mathrm{h}})\psi_k^{\mathrm{he}}(t) - (1 - f_k^{\mathrm{e}} - f_k^{\mathrm{h}})(d_k^{\mathrm{eh}}E(t) + \Sigma_{k'}\ W_{k,k'}^{\mathrm{eh}}\psi_{k'}^{\mathrm{he}}(t)) \quad (1)$$

with a weak external probe field $E(t)$ incident perpendicular on the TMDC heterobilayer. The photoexcited electrons and holes generated by a strong pump field are described in quasi-equilibrium by Fermi distribution functions $f_k^a$. The linear susceptibility

$$\chi(\omega) = \Sigma_{k,\mathrm{eh}}\ \psi_k^{\mathrm{he}}(\omega)d_k^{\mathrm{eh}}/E(\omega) \quad (2)$$

in the frequency domain is used in a second step to derive reflectance and absorptance spectra, as detailed below.

In the SBE, material properties enter via band structures $\varepsilon_k^a$, screened Coulomb matrix elements $W_{\mathrm{q}}$ and dipole matrix elements $d_{\mathrm{k}}$. Band structure renormalizations due to photoexcited carriers are given by the screened-exchange-Coulomb-hole self-energy $\Sigma_{k,\mathrm{SXCH}}^a$, while plasma screening is described by a dielectric function in the long-wavelength approximation via $W_{k,k'}^{\mathrm{ab}} = \varepsilon_{k-k',\mathrm{pl}}^{-1}V_{k,k'}^{\mathrm{ab}}$ (*31*). The band structure of the unexcited $MoSe_2$-$WSe_2$ heterolayer is modeled under an effective mass approximation for the relevant conduction and valence band valleys as shown in fig. S8. The energetic ordering of the bands is inspired by first-principle calculations (*14*) while we adjust the band edges to match our experimental reflectance spectra. We assume that the effective masses are approximately given by the masses of the respective monolayers as provided in (*32*). For the $Q$ and Γ valleys, we average over both materials. The band edges and masses are collected in table S1.

The Coulomb interaction between carriers located in different TMD layers is significantly weaker than the intralayer Coulomb interaction due to the spatial separation of carriers in growth direction. To account for this effect, we use model Coulomb matrix elements in a 2D layer basis $|\alpha\rangle = \{|\mathrm{MoSe_2}\rangle, |\mathrm{WSe_2}\rangle\}$

$$V_{k,k}^{ab} = \Sigma_{\alpha,\beta}\ c_\alpha^a(k)c_\beta^{-b}(k')c_\beta^b(k)c_\alpha^a(k')V_{k-k'}^{\alpha\beta} \quad (3)$$

where the contribution of a certain layer α to the band a is given by $|c_\alpha^{\mathrm{a}}(k)|^2$. We assign layer contributions according to the first-principle results in (*14*) as given in table S1. The matrix elements $V_{\mathrm{q}}^{\alpha\beta}$ are modeled by a macroscopic dielectric function $\varepsilon_{\mathrm{q,b}}^{-1,\alpha\beta}$ and a form factor $F_{\mathrm{q}}^{\alpha\beta}$ according to

$$V_{\mathrm{q}}^{\alpha\beta} = \frac{e^2}{2\varepsilon_0 \mathrm{q}}\varepsilon_{\mathrm{q,b}}^{-1,\alpha\beta}F_{\mathrm{q}}^{\alpha\beta} \quad (4)$$

The dielectric function for each layer combination is obtained by solving Poisson's equation for the respective dielectric structure (*33*) as shown in fig. S9. The dielectric constants of the TMD materials are computed as geometric mean of the values given in (*34*), where also layer widths are provided. The dielectric constant of h-BN is taken

from (*35*). The layer substrate distance $h_1$ = 0.5 nm has been found to be an appropriate value in (*33*), while we assume that the two TMD layers are slightly closer to each other using $h_2$ = 0.3 nm. The form factor accounts for the confinement of carriers inside the atomically thin layers via the confinement functions $\xi^{\alpha}(z)$

$$F_q^{\alpha\beta} = \int dz \int dz' \xi^{\alpha}(z)\xi^{\beta}(z')e^{-q|z-z'|}\xi^{\beta}(z')\xi^{\alpha}(z) \quad (5)$$

For the confinement functions, we assume eigenfunctions of the infinitely deep potential well with two nodes due to the mostly d-like character of electronic orbitals.

To describe light-matter interaction, we assume a circularly polarized electric field selecting dipoles in the *K* valley between like-spin bands. The numerical values for the intralayer dipoles are computed using the simple lattice model from (*36*), where we neglect the momentum dependence. For the interlayer transition dipoles, we assume a value that is 10 times smaller than that in the $MoSe_2$ monolayer (*28*).

The SBE contains a phenomenological damping factor γ, which corresponds to the HWHM of lines in optical spectra. Because of excitation-induced dephasing, γ depends on the actual excited carrier density. We fix the value of γ at different densities by matching simulated and experimental reflectance spectra. For the intralayer $MoSe_2$ transition, this yields γ = 25 meV for carrier density $n = 1.3 \times 10^{12}$ cm$^{-2}$, γ = 30 meV for $n = 1.9 \times 10^{12}$ cm$^{-2}$, γ = 35 meV for $n = 5.3 \times 10^{12}$ cm$^{-2}$, and γ = 50 meV for $n = 3.13 \times 10^{13}$ cm$^{-2}$. For the intralayer $WSe_2$ transition, we use a γ that is 50% larger to account for the stronger dephasing, in accordance with the experimental reflectance spectra.

Figure 4A shows simulated transient reflectance spectra at excitation densities $n_0 = 6 \times 10^{11}$, $4 \times 10^{12}$, and $3 \times 10^{13}$ cm$^{-2}$ obtained from theoretical optical absorptance and the experimental sample geometry. Also shown as comparison are experimental transient reflectance spectra ($\Delta t$ = 1 ps) at similar $n_0$ values Fig. 4B. The simulations and experimental spectra are in excellent agreement, including main features of bleaching of intralayer excitonic transitions for all excitation densities, the broad induced absorption feature above the Mott density, and stimulated emission near the renormalized bandgap at ~1.3 eV. This agreement provides strong support for the conclusion on Mott transition from the interlayer exciton to charge-separated e/h plasmas and for the calibration of carrier density in the CW measurement in Fig. 1.

Figure 4C shows calculated absorptance spectra at selected $n_{eh}$ values. By determining at which $n_{eh}$ excitonic absorption resonance becomes bleached, we find $n_{Mott} = 3 \times 10^{12}$ cm$^{-2}$. This value is close to $n_{Mott} = 1.6 \times 10^{12}$ cm$^{-2}$ obtained from an analytical estimate (*29*) of $a_0 n_{Mott}^{1/2} \approx 0.25$ and an interlayer exciton radius of ~2 nm (*14*). More specifically, we follow excitonic absorption where exciton features gradually fade through broadening from a clear peak to transparency and eventually to gain (*24*, *37*). Below $n_{Mott}$, the presence of excitons significantly reduces scattering. There is an accelerated broadening after excitons cease to exist above $n_{Mott}$ (*24*), and this leaves a signature in increased PL linewidth. Note that the observed increase in PL peak width above the Mott density is much larger than what was observed before in coupled III–V quantum wells (*11*, *12*). The interlayer excitons in the 2D TMDC heterobilayer (*7*–*10*) are much more strongly bound and less Coulomb screened than their counterparts in III–V coupled quantum wells (*11*, *12*); as a result, the Mott transition has a much larger effect on reducing Coulomb screening in the former.

In addition to revealing the Mott threshold from the disappearance of sharp excitonic features, the theoretical absorption spectra show the decrease in oscillator strength with increasing $n_{eh}$, as expected from Pauli blocking and screening effects. Optical transparency is reached at $n_{eh}$ ~$4 \times 10^{14}$ cm$^{-2}$, above which stimulated emission dominates. On the basis of the calculated optical spectra, we obtain the $n_{eh}$-dependent relative absorptance ($\sigma/\sigma_0$, where $\sigma_0$ is the absorptance at the low $n_{eh}$ limit) shown in Fig. 4D for two photon energies. These calculated results are used in the calibration of experimental excitation densities (see fig. S7).

## Mechanisms of interlayer PL emission from the heterobilayer

We now turn to the mechanism of PL emission from interlayer excitons and charge-separated e/h plasmas. A comparison of TRPL in Fig. 2 and transient reflectance in Fig. 3 reveals a major discrepancy in the time scales involved. PL decays are characterized by time constants of ~$10^2$ ns, but transient reflectance features time constants in the range of $10^{1\text{-}2}$ ps. We show kinetic profiles (vertical cuts of transient reflectance spectra) for two representative probe energies, hν = 1.351 and 1.624 eV, for induced absorption (Fig. 3G) and photobleaching (Fig. 3H), respectively. Figure 3G shows little induced absorption at hν = 1.351 eV for $n_0 = 1.0 \times 10^{11}$ and $9.6 \times 10^{11}$ cm$^{-2}$, as expected from the absence of plasmas. When $n_0$ is increased above $n_{Mott}$, we observe both positive (induced absorption) and negative (stimulated emission) $\Delta R/R_0$ signal, consistent with the transformation to the charge-separated plasmas region. For the intermediate density $n_0 = 5.6 \times 10^{12}$ cm$^{-2}$, stimulated emission dominates. At the highest density of $n_0 = 3.4 \times 10^{13}$ cm$^{-2}$,

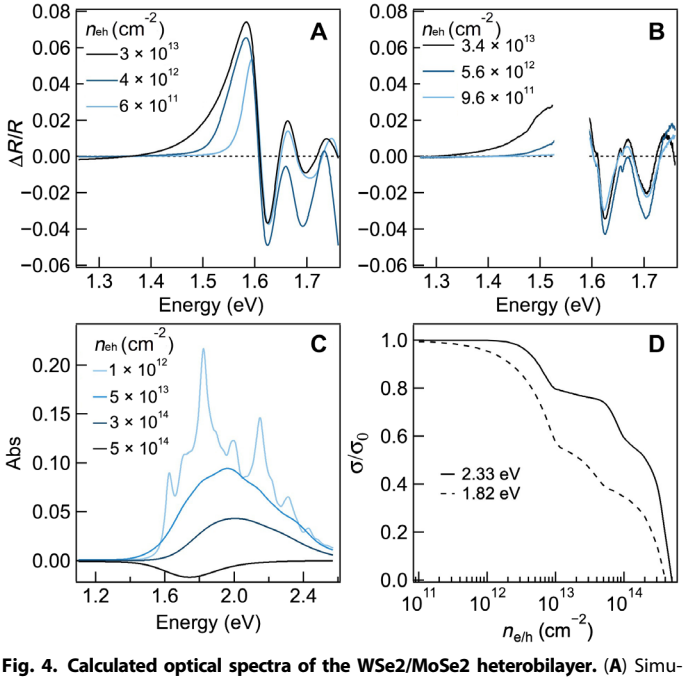


**Fig. 4. Calculated optical spectra of the WSe2/MoSe2 heterobilayer.** (**A**) Simulated reflectance spectra from theoretical optical spectra and experimental sample geometry at the indicated excitation densities ($n_{eh} = 6 \times 10^{11}$ to $3 \times 10^{13}$ cm$^{-2}$). (**B**) Experimental reflectance spectra at $\Delta t$ = 1 ps at initial excitation densities of $n_0 = 9.6 \times 10^{11}$ to $3.4 \times 10^{13}$ cm$^{-2}$. (**C**) Calculated optical absorptance spectra at $n_{eh} = 1 \times 10^{11}$ to $5 \times 10^{14}$ cm$^{-2}$. (**D**) Calculated relative optical absorptance as a function of $n_{eh}$ at two photon energies used in the experiments.

induced absorption dominates at $\Delta t < 60$ ps and stimulated emission at $\Delta t > 60$ ps.

The kinetics profiles at hν = 1.624 eV (Fig. 3H) reveal the short-time nature of photobleaching. At $n_0 = 1.0 \times 10^{11}$, $9.6 \times 10^{11}$, and $5.6 \times 10^{12}$ cm$^{-2}$, photobleaching ($-\Delta R/R_0$) grows with time constants of $\tau_1 = 140 \pm 30$ fs, attributed to the ultrafast dissociation of intralayer excitons in each TMDC monolayer to form charge-separated states that increase the Pauli blocking effect. The photobleaching intensity peaks in subpicoseconds and decays on longer time scales. At $n_0 \leq n_{Mott}$ ($1.0 \times 10^{11}$ and $9.6 \times 10^{11}$ cm$^{-2}$), bleaching intensity decays with time constants of $\tau_2 = 30 \pm 10$ ps. This time constant increases above $n_{Mott}$ to $\tau_2 = 90 \pm 30$ ps and $\tau_2 = 290 \pm 60$ ps at $n_0 = 5.6 \times 10^{12}$ and $3.4 \times 10^{13}$ cm$^{-2}$, respectively. There is a three order of magnitude difference between the time constants for PL decay ($\tau_{PL}$) and those of photobleaching recovery ($\tau_2$). The fast recovery in photobleaching cannot result from the loss of photoexcited charge carriers to recombination but rather to the scattering of these carriers away from the *K* valley. Computational studies on the $WSe_2/MoSe_2$ heterobilayer have shown that the conduction band is lower in energy at the *Q* point than that at the *K* point, while valence band energy at the Γ point is close in energy to that of the *K* point (*14*). Following charge separation, intervalley scattering transfers carrier populations in the *K* valleys to the *Q* and Γ valleys. This process reduces Pauli blocking of optical transitions in the *K* valleys and accounts for the $\tau_2 = 30$ to 290 ps decay time constants. Efficient intervalley carrier scattering involves optical phonons, and its rate is decreased by screening as excitation density is increased, thus accounting for longer $\tau_2$ at higher $n_0$ above $n_{Mott}$. The *Q* and Γ valleys serve as carrier reservoirs; the momentum-indirect nature prohibits radiative recombination of electrons and holes in these valleys. Instead, scattering of electrons and holes back to the *K* valleys likely occurs before radiative recombination happens. This explains the long PL lifetimes on the $10^2$ ns time scale. In a similar proposal, dark traps have been suggested as exciton reservoirs for slow PL emission in monolayer $MoS_2$ (*38*).

## DISCUSSION

The results presented here establish photoinduced charge separation at van der Waals interfaces as an effective means to control 2D charge carrier densities. Using the heterobilayer of $WSe_2/MoSe_2$, we show the spectroscopic signature of Mott transition from interlayer excitons to charge-separated e/h plasmas, in excellent agreement with calculation based on a fully microscopic quantum theory. We point out that the spectroscopy measurements probe the combined responses of the electron and hole plasmas across the heterobilayer interface. Resolving the individual response of the electron or hole plasma is challenging but possible with time and angle-resolved photoemission spectroscopy, which is underway in our laboratory (*39*). The combined PL and transient reflectance measurements also reveal the participation of intervalley scattering and dark exciton/carrier reservoirs in radiative recombination dynamics. Photoinduced charge separation under CW conditions allows us to reach charge carrier densities as high as ~$4 \times 10^{14}$ cm$^{-2}$, which is two orders of magnitude above the Mott density and is at the same level demonstrated previously for gate-doped superconductivity in TMDCs (*1*–*4*). These findings suggest that photoinduced charge separation at van der Waals interfaces is an effective means to realize complex electronic phases in 2D materials, particularly photoinduced superconductivity under CW conditions.

## MATERIALS AND METHODS

### Preparation of 2D $WSe_2/MoSe_2$ heterobilayer samples

Monolayers of $WSe_2$ and $MoSe_2$ were mechanically exfoliated from bulk crystals grown by the self-flux method. These monolayers had low defect densities (<$10^{11}$ cm$^{-2}$) (*16*). h-BN flakes of thicknesses 5 to 35 nm and of flat surfaces were also obtained by mechanical exfoliation. The flakes ($WSe_2$, $MoSe_2$, and BN) were characterized by atomic force microscopy and Raman spectroscopy.

The crystal orientations of $WSe_2$ and $MoSe_2$ monolayers were determined by second harmonic generation (SHG) measurement on an inverted optical microscope (Olympus IX73). Linearly polarized femtosecond laser light (Coherent Mira 900, 80 MHz, 800 nm, 100 fs) was focused onto a monolayer with a 100×, numerical aperture (NA) 0.80 objective (Olympus LMPLFLN100X). The reflected SHG signal at 400 nm was collected by the same objective, filtered by a short-pass dichroic mirror, short-pass and band-pass filters, and a Glan-Taylor linear polarizer; detected by a photomultiplier tube (R4220P, Hamamatsu); and recorded by a photon counter (SR400, Stanford Research Systems). We obtained the azimuthal angular (θ) distribution of SHG signal by rotating either the sample (*40*) or the laser polarization (*41*) (via a half waveplate) with fixed polarization detection. Because of the $D_{3h}$ symmetry, the nonvanishing tensor elements of the second-order susceptibility of $WSe_2$ and $MoSe_2$ monolayers are $\chi^{(2)}_{yyy} = -\chi^{(2)}_{yxx} = -\chi^{(2)}_{xxy} = -\chi^{(2)}_{xyx}$, where the *x* axis is defined as the zigzag direction. When we rotated the sample, the SHG intensity showed sixfold symmetry: $I_\perp \propto \cos^2(3\theta)$ and $I_\parallel \propto \sin^2(3\theta)$, where θ is the angle between the laser polarization and the zigzag direction. When we rotated the laser polarization, the SHG intensity showed fourfold symmetry: $I_y \propto \cos^2(2\theta)$ and $I_x \propto \sin^2(2\theta)$. We used triangular flakes of monolayer $WS_2$ (6Carbon) or $MoS_2$ (2DLayer), where zigzag directions are the same as crystal edges, both grown from chemical vapor deposition, to calibrate the SHG setup.

The 2D $WSe_2/MoSe_2$ heterobilayer was prepared by the polymer-free van der Waals assembly technique (*42*). A transparent polydimethylsiloxane stamp coated by a thin layer of polypropylene carbonate (PPC) was used to pick up a thin layer of exfoliated h-BN. This h-BN was then used to pick up the first TMDC monolayer. The second TMDC monolayer was aligned to and picked up by the first monolayer on a high-precision rotation stage. The heterostructure was finally stamped onto a thicker layer of h-BN and detached from the PPC at elevated temperatures (90° to 120°C). The residual PPC was washed away by acetone to give a clean h-BN/$MoSe_2$/$WSe_2$/h-BN heterostructure on the Si/SiO2 substrate.

Figure S1 shows optical microscope images of the two BN/$WSe_2$/$MoSe_2$/BN heterobilayer samples used in the spectroscopy measurements shown in the main text. Figures S2 and S3 show SHG polarization data used to determine the two alignment angles, $\theta = 4° \pm 2°$ and $13° \pm 2°$, respectively.

### Steady-state and time-resolved PL measurements

All spectroscopic measurements were performed on a home-built reflection microscope system based on a liquid-helium recirculating optical cryostat (Montana Instruments Fusion/X-Plane) with a 100×, NA 0.75 objective (Zeiss LD EC Epiplan-Neofluar 100×/0.75 HD DIC M27). The temperature of the sample stage could be varied between 3 and 350 K. In all experiments presented in this study, the TMDC heterobilayer and monolayer samples were at 4 K in a vacuum (<$10^{-6}$ torr) environment, unless otherwise noted.

In steady-state PL measurements, a CW laser (532 nm) was focused by the objective to a diffraction-limited spot on the sample. The excitation power was measured by a calibrated power meter (OPHIR StarLite) with broad dynamic range. The PL light was collected by the same objective, spectrally filtered, dispersed by a grating, and detected by an InGaAs photodiode array (PyLoN-IR, Princeton Instruments). The wavelength was calibrated by neon-argon and mercury atomic emission sources (IntelliCal, Princeton Instruments). The intensity was calibrated by three independent NIST traceable light sources: a 400 to 1050-nm tungsten halogen lamp (StellarNet SL1-CAL), a 250 to 2400-nm quartz tungsten halogen lamp (Oriel 63355), and a 425 to 1000-nm LED (light-emitting diode) (IntelliCal, Princeton Instruments).

In TRPL measurements, the pulsed excitation light ($h\nu$ = 1.82 eV; pulse duration, 150 fs) was from a wavelength tunable output of an visible optical parametric amplifier (Coherent OPA 9450) pumped by a Ti:sapphire regenerative amplifier (Coherent RegA 9050, 250 kHz, 800 nm, 100 fs). The interlayer PL emission in the 900 to 1000-nm region was selected and focused onto a single-photon avalanche photodiode (IDQ ID100-50). The TRPL trace was collected with a time-correlated single-photon counting module (Becker & Hickl GmbH SPC-130). The instrument response function, determined by collecting scattered laser light, has an FWHM of 100 ps (fig. S5). The time resolution of TRPL was estimated at ~20% of the FWHM, i.e., ~20 ps.

### Reflectance and transient reflectance measurements

In reflectance measurements, the broadband white light was directed to the sample with the objective, reflected, collected by the same objective, and detected by an InGaAs photodiode array (PyLoN-IR, Princeton Instruments). For the reflectance at the low-density limit, the spectrally filtered and collimated white light from a 3200 K halogen lamp (KLS EKE/AL) was used. Reflectance was also taken for the white light probe in the same geometry as transient reflectance to confirm that it is in the linear regime. A 150-nm gold film deposited by electron beam evaporation on the same $Si/SiO_2$ substrate was used as a reflectance standard.

In transient reflectance measurements, femtosecond laser pulses from the Ti:sapphire regenerative amplifier (Coherent RegA 9050, 250 kHz, 800 nm, 100 fs) was split into two beams: One was used to pump the visible optical parametric amplifier (Coherent OPA 9450) to generate tunable pump light, and the other was focused onto a sapphire crystal to generate white light continuum probe light. The pump was then chirp compensated by a prism pair, delayed by a motorized translation stage, modulated by an optical chopper, combined with the probe, and directed collinearly to the sample by the objective. To achieve homogenous excitation, average over a sufficient area, and reduce nonlinear effect of probe, both beams were focused onto the back focal plane of the objective to obtain a large beam diameter at the sample plane, unless otherwise specified. The reflected probe light was then collected by the same objective, spectrally filtered to remove pump light, and recorded with the InGaAs photodiode array (PyLoN-IR, Princeton Instruments). This detector was synchronized with the optical chopper through a home-made frequency doubler. At each specific pump-probe delay, the reflected probe spectra with and without pump was recorded, and the transient reflectance ($\Delta R/R$) was calculated. We determined the sign of the transient reflectance signal by recording the chopper output with a data acquisition board (National Instruments) triggered by the InGaAs detector. The chopper modulation frequency was selected to maximize the signal-to-noise ratio of transient reflectance signal.

## SUPPLEMENTARY MATERIALS

Supplementary material for this article is available at http://advances.sciencemag.org/cgi/content/full/5/9/eaax0145/DC1

Supplementary Text

Fig. S1. 2D $MoSe_2/WSe_2$ heterostructure samples.

Fig. S2. Determination of monolayer orientation via polarization-resolved SHG.

Fig. S3. Determination of monolayer orientation via polarization-resolved SHG: The case of rotating laser polarization.

Fig. S4. Low-temperature spectroscopy-microscopy setup.

Fig. S5. Time resolution of TRPL and pump-probe experiments.

Fig. S6. Calculated optical absorptances for monolayer $WSe_2$, monolayer $MoSe_2$, and $WSe_2/MoSe_2$ heterobilayer based on the reported dielectric constants in (*17*).

Fig. S7. Calibration of steady-state excitation density.

Fig. S8. Band structure model for the AA-stacked $MoSe_2$-$WSe_2$ heterolayer, including the high-symmetry points $\Gamma$ and *K*, as well as the *Q* point in between.

Fig. S9. Dielectric structure model.

Fig. S10. PL of the misaligned heterostructure.

Fig. S11. Comparison of steady-state and pulsed PL spectra at similar carrier densities.

Fig. S12. Excitation density and temperature-dependent PL spectra from the $WSe_2/MoSe_2$ heterobilayer.

Fig. S13. BN-encapsulated monolayer $MoSe_2$ and $WSe_2$ samples.

Fig. S14. Electron-hole plasma dynamics in monolayers by transient reflectance.

Table S1. Band edges, effective masses, and layer contributions for the AA-stacked $MoSe_2$-$WSe_2$ heterolayer according to the notation in fig. S8.

References (*43*–*49*)

## REFERENCES AND NOTES


1. L. J. Li, E. C. T. O'Farrell, K. P. Loh, G. Eda, B. Özyilmaz, A. H. C. Neto, Controlling many-body states by the electric-field effect in a two-dimensional material. *Nature* **529**, 185–189 (2016).
2. Y. Saito, Y. Nakamura, M. S. Bahramy, Y. Kohama, J. Ye, Y. Kasahara, Y. Nakagawa, M. Onga, M. Tokunaga, T. Nojima, Y. Yanase, Y. Iwasa, Superconductivity protected by spin–valley locking in ion-gated $MoS_2$. *Nat. Phys.* **12**, 144–149 (2016).
3. J. M. Lu, O. Zheliuk, I. Leermakers, N. F. Q. Yuan, U. Zeitler, K. T. Law, J. T. Ye, Evidence for two-dimensional Ising superconductivity in gated $MoS_2$. *Science* **350**, 1353–1357 (2015).
4. J. M. Lu, O. Zheliuk, Q. Chen, I. Leermakers, N. E. Hussey, U. Zeitler, J. Ye, Full superconducting dome of strong Ising protection in gated monolayer $WS_2$. *Proc. Natl. Acad. Sci. U.S.A.* **115**, 3551–3556 (2018).
5. X. Hong, J. Kim, S.-F. Shi, Y. Zhang, C. Jin, Y. Sun, S. Tongay, J. Wu, Y. Zhang, F. Wang, Ultrafast charge transfer in atomically thin $MoS_2/WS_2$ heterostructures. *Nat. Nanotechnol.* **9**, 682–686 (2014).
6. H. Zhu, J. Wang, Z. Gong, Y. D. Kim, J. Hone, X.-Y. Zhu, Interfacial charge transfer circumventing momentum mismatch at two-dimensional van der Waals heterojunctions. *Nano Lett.* **17**, 3591–3598 (2017).
7. P. Rivera, J. R. Schaibley, A. M. Jones, J. S. Ross, S. Wu, G. Aivazian, P. Klement, K. Seyler, G. Clark, N. J. Ghimire, J. Yan, D. G. Mandrus, W. Yao, X. Xu, Observation of long-lived interlayer excitons in monolayer $MoSe_2$–$WSe_2$ heterostructures. *Nat. Commun.* **6**, 6242 (2015).
8. J. Kunstmann, F. Mooshammer, P. Nagler, A. Chaves, F. Stein, N. Paradiso, G. Plechinger, C. Strunk, C. Schüller, G. Seifert, D. R. Reichman, T. Korn, Momentum-space indirect interlayer excitons in transition-metal dichalcogenide van der Waals heterostructures. *Nat. Phys.* **14**, 801–805 (2018).
9. J. Kim, C. Jin, B. Chen, H. Cai, T. Zhao, P. Lee, S. Kahn, K. Watanabe, T. Taniguchi, S. Tongay, M. F. Crommie, F. Wang, Observation of ultralong valley lifetime in $WSe_2/MoS_2$ heterostructures. *Sci. Adv.* **3**, e1700518 (2017).
10. P. Rivera, H. Yu, K. L. Seyler, N. P. Wilson, W. Yao, X. Xu, Interlayer valley excitons in heterobilayers of transition metal dichalcogenides. *Nat. Nanotechnol.* **13**, 1004–1015 (2018).
11. M. Stern, V. Garmider, V. Umansky, I. Bar-Joseph, Mott transition of excitons in coupled quantum wells. *Phys. Rev. Lett.* **100**, 256402 (2008).
12. G. Kiršanskė, P. Tighineanu, R. S. Daveau, J. Miguel-Sánchez, P. Lodahl, S. Stobbe, Observation of the exciton Mott transition in the photoluminescence of coupled quantum wells. *Phys. Rev. B* **94**, 155438 (2016).
13. A. Chernikov, C. Ruppert, H. M. Hill, A. F. Rigosi, T. F. Heinz, Population inversion and giant bandgap renormalization in atomically thin $WS_2$ layers. *Nat. Photonics* **9**, 466–470 (2015).
14. R. Gillen, J. Maultzsch, Interlayer excitons in $MoSe_2/WSe_2$ heterostructures from first principles. *Phys. Rev. B* **97**, 165306 (2018).
15. H. Yu, Y. Wang, Q. Tong, X. Xu, W. Yao, Anomalous light cones and valley optical selection rules of interlayer excitons in twisted heterobilayers. *Phys. Rev. Lett.* **115**, 187002 (2015).

16. D. Edelberg, D. Edelberg, D. Rhodes, A. Kerelsky, B. Kim, J. Wang, A. Zangiabadi, C. Kim, A. Abhinandan, J. Ardelean, M. Scully, D. Scullion, L. Embon, I. Zhang, R. Zu, E. J. G. Santos, L. Balicas, C. Marianetti, K. Barmak, X.-Y. Zhu, J. Hone, A. N. Pasupathy, Hundredfold enhancement of light emission via defect control in monolayer transition-metal dichalcogenides. arXiv:1805.00127 (2018).
17. Y. Li, A. Chernikov, X. Zhang, A. Rigosi, H. M. Hill, A. M. van der Zande, D. A. Chenet, E.-M. Shih, J. Hone, T. F. Heinz, Measurement of the optical dielectric function of monolayer transition-metal dichalcogenides: $MoS_2$, $MoSe_2$, $WS_2$, and $WSe_2$. *Phys. Rev. B* **90**, 205422 (2014).
18. J. S. Ross, S. Wu, H. Yu, N. J. Ghimire, A. M. Jones, G. Aivazian, J. Yan, D. G. Mandrus, D. Xiao, W. Yao, X. Xu, Electrical control of neutral and charged excitons in a monolayer semiconductor. *Nat. Commun.* **4**, 1474 (2013).
19. Z. Ye, L. Waldecker, E. Y. Ma, D. Rhodes, A. Antony, B. Kim, X.-X. Zhang, M. Deng, Y. Jiang, Z. Lu, D. Smirnov, K. Watanabe, T. Taniguchi, J. Hone, F. Heinz, Efficient generation of neutral and charged biexcitons in encapsulated $WSe_2$ monolayers. *Nat. Commun.* **9**, 3718 (2018).
20. M. Barbone, A. R.-P. Montblanch, D. M. Kara, C. Palacios-Berraquero, A. R. Cadore, D. De Fazio, B. Pingault, E. Mostaani, H. Li, B. Chen, K. Watanabe, T. Taniguchi, S. Tongay, G. Wang, A. C. Ferrari, M. Atatüre, Charge-tuneable biexciton complexes in monolayer $WSe_2$. *Nat. Commun.* **9**, 3721 (2018).
21. S.-Y. Chen, T. Goldstein, T. Taniguchi, K. Watanabe, J. Yan, Coulomb-bound four- and five-particle intervalley states in an atomically-thin semiconductor. *Nat. Commun.* **9**, 3717 (2018).
22. P. Rivera, K. L. Seyler, H. Yu, J. R. Schaibley, J. Yan, D. G. Mandrus, W. Yao, X. Xu, Valley-polarized exciton dynamics in a 2D semiconductor heterostructure. *Science* **351**, 688–691 (2016).
23. M. Stern, V. Umansky, I. Bar-Joseph, Exciton liquid in coupled quantum wells. *Science* **343**, 55–57 (2014).
24. R. P. Smith, J. K. Wahlstrand, A. C. Funk, R. P. Mirin, S. T. Cundiff, J. T. Steiner, M. Schafer, M. Kira, S. W. Koch, Extraction of many-body configurations from nonlinear absorption in semiconductor quantum wells. *Phys. Rev. Lett.* **104**, 247401 (2010).
25. S. Chatterjee, C. Ell, S. Mosor, G. Khitrova, H. M. Gibbs, W. Hoyer, M. Kira, S. W. Koch, J. P. Prineas, H. Stolz, Excitonic photoluminescence in semiconductor quantum wells: Plasma versus excitons. *Phys. Rev. Lett.* **92**, 067402 (2004).
26. B. Miller, A. Steinhoff, B. Pano, J. Klein, F. Jahnke, A. Holleitner, U. Wurstbauer, Long-lived direct and indirect interlayer excitons in van der Waals heterostructures. *Nano Lett.* **17**, 5229–5237 (2017).
27. K. F. Mak, M. Y. Sfeir, Y. Wu, C. H. Lui, J. A. Misewich, T. F. Heinz, Measurement of the optical conductivity of graphene. *Phys. Rev. Lett.* **101**, 196405 (2008).
28. J. S. Ross, P. Rivera, J. Schaibley, E. Lee-Wong, H. Yu, T. Taniguchi, K. Watanabe, J. Yan, D. Mandrus, D. Cobden, W. Yao, X. Xu, Interlayer exciton optoelectronics in a 2D heterostructure p-n junction. *Nano Lett.* **17**, 638–643 (2017).
29. L. Meckbach, T. Stroucken, S. W. Koch, Giant excitation induced bandgap renormalization in TMDC monolayers. *Appl. Phys. Lett.* **112**, 061104 (2018).
30. H. Haug, S. W. Koch, *Quantum Theory of the Optical and Electronic Properties of Semiconductors* (World Scientific, 2009).
31. A. Steinhoff, M. Rosner, F. Jahnke, T. O. Wehling, C. Gies, Influence of excited carriers on the optical and electronic properties of $MoS_2$. *Nano Lett.* **14**, 3743–3748 (2014).
32. A. Kormányos, G. Burkard, M. Gmitra, J. Fabian, V. Zólyomi, N. D Drummond, V. Fal'ko, k·p theory for two-dimensional transition metal dichalcogenide semiconductors. arXiv:1410.6666 (2015).
33. M. Florian, M. Hartmann, A. Steinhoff, J. Klein, A. W. Holleitner, J. J. Finley, T. O. Wehling, M. Kaniber, C. Gies, The dielectric impact of layer distances on exciton and trion binding energies in van der Waals heterostructures. *Nano Lett.* **18**, 2725–2732 (2018).
34. I. Kylänpää, H.-P. Komsa, Binding energies of exciton complexes in transition metal dichalcogenide monolayers and effect of dielectric environment. *Phys. Rev. B* **92**, 205418 (2015).
35. R. Geick, C. H. Perry, G. Rupprecht, Normal modes in hexagonal boron nitride. *Phys. Rev.* **146**, 543 (1966).
36. D. Xiao, G.-B. Liu, W. Feng, X. Xu, W. Yao, Coupled spin and valley physics in monolayers of $MoS_2$ and other group-VI dichalcogenides. *Phys. Rev. Lett.* **108**, 196802 (2012).
37. E. J. Sie, E. J. Sie, A. Steinhoff, C. Gies, C. H. Lui, Q. Ma, M. Rösner, G. Schönhoff, F. Jahnke, T. O. Wehling, Y.-H. Lee, J. Kong, P. Jarillo-Herrero, N. Gedik, Observation of exciton redshift-blueshift crossover in monolayer $WS_2$. *Nano Lett.* **17**, 4210–4216 (2017).
38. A. J. Goodman, A. P. Willard, W. A. Tisdale, Exciton trapping is responsible for the long apparent lifetime in acid-treated $MoS_2$. *Phys. Rev. B* **96**, 121404 (2017).
39. F. Liu, M. Ziffer, K. R. Hansen, J. Wang, X. Zhu, Direct determination of band gap renormalization in photo-excited monolayer $MoS_2$. *Phys. Rev. Lett.* **122**, 246803 (2019).
40. Y. Li, Y. Li, Y. Rao, K. F. Mak, Y. You, S. Wang, C. R. Dean, T. F. Heinz, Probing symmetry properties of few-layer $MoS_2$ and h-BN by optical second-harmonic generation. *Nano Lett.* **13**, 3329–3333 (2013).
41. E. Mannebach, K. Duerloo, E. M. Mannebach, K.-A. N. Duerloo, L. A. Pellouchoud, M.-J. Sher, S. Nah, Y.-H. Kuo, Y. Yu, A. F. Marshall, L. Cao, E. J. Reed, A. M. Lindenberg, Ultrafast electronic and structural response of monolayer $MoS_2$ under intense photoexcitation conditions. *Acs Nano.* **8**, 10734–10742 (2014).
42. L. Wang, I. Meric, P. Y. Huang, Q. Gao, Y. Gao, H. Tran, T. Taniguchi, K. Watanabe, L. M. Campos, D. A. Muller, J. Guo, P. Kim, J. Hone, K. L. Shepard, C. R. Dean, One-dimensional electrical contact to a two-dimensional material. *Science* **342**, 614–617 (2013).
43. A. Laturia, M. L. Van de Put, W. G. Vandenberghe, Dielectric properties of hexagonal boron nitride and transition metal dichalcogenides: From monolayer to bulk. *npj 2D Mater. Appl.* **2**, 6 (2018).
44. M. Kira, F. Jahnke, H. S. W. Koch, Quantum theory of spontaneous emission and coherent effects in semiconductor microstructures. *Prog. Quantum Electron.* **23**, 189–279 (1999).
45. D. E. Aspnes, J. B. Theeten, Spectroscopic analysis of the interface between Si and its thermally grown oxide. *J. Electrochem. Soc.* **127**, 1359–1365 (1980).
46. I. H. Malitson, Interspecimen comparison of the refractive index of fused silica. *J. Opt. Soc. Am.* **55**, 1205–1209 (1965).
47. A. Segura, L. Artús, R. Cuscó, T. Taniguchi, G. Cassabois, B. Gil, Natural optical anisotropy of h-BN: Highest giant birefringence in a bulk crystal through the mid-infrared to ultraviolet range. *Phys. Rev. Mater.* **2**, 024001 (2018).
48. G. Wang, X. Marie, I. Gerber, T. Amand, D. Lagarde, L. Bouet, M. Vidal, A. Balocchi, B. Urbaszek, Giant enhancement of the optical second-harmonic emission of $WSe_2$ monolayers by laser excitation at exciton resonances. *Phys. Rev. Lett.* **114**, 097403 (2015).
49. G. Wang, I. C. Gerber, L. Bouet, D. Lagarde, A. Balocchi, M. Vidal, T. Amand, X. Marie, B. Urbaszek, Exciton states in monolayer $MoSe_2$: Impact on interband transitions. *2D Mater.* **2**, 045005 (2015).

**Acknowledgments**

**Funding:** The transient reflectance and CW-PL measurements were supported by the National Science Foundation (NSF) grant DMR-1608437 (to X.-Y.Z. and J.H.). The TRPL measurements were supported by NSF grant DMR-1809680 (to X.-Y.Z.). Sample preparation, purchase of the recirculating He-cryostat, and optical setup were supported by the Center for Precision Assembly of Superstratic and Superatomic Solids, a Materials Science and Engineering Research Center (MRSEC) through NSF grant DMR-1420643. The control experiments on charge separation in the misaligned heterojunction (fig. S10) were supported by the Office of Naval Research under award no. N00014-16-1-2921. A.S., M.F., and F.J. acknowledge support for the theoretical calculation from the Deutsche Forschungsgemeinschaft (RTG 2247 Quantum Mechanical Materials Modelling) and resources for computational time at the HLRN (Hannover/Berlin). **Author contributions:** X.-Y.Z. and J.H. conceived this work. J.W., J.A., and Y.B. performed the experiments. A.S. and M.F. carried out the theoretical calculations with supervision from M.K. and F.J. X.X. participated in the interpretation of the experimental findings. X.-Y.Z., M.K., and J.H. wrote the manuscript with inputs from all coauthors. All authors read and commented on the manuscript. **Competing interests:** The authors declare that they have no competing interests. **Data and materials availability:** All data needed to evaluate the conclusions in the paper are present in the paper and/or the Supplementary Materials. Additional data related to this paper may be requested from the authors.

Submitted 14 February 2019
Accepted 14 August 2019
Published 13 September 2019
10.1126/sciadv.aax0145

**Citation:** J. Wang, J. Ardelean, Y. Bai, A. Steinhoff, M. Florian, F. Jahnke, X. Xu, M. Kira, J. Hone, X.-Y. Zhu, Optical generation of high carrier densities in 2D semiconductor heterobilayers. *Sci. Adv.* **5**, eaax0145 (2019).